Cutanda-Henriquez, V.; Garcia Chocano, VM.; Sánchez-Dehesa Moreno-Cid, J. (2017). Viscothermal Losses in Double-Negative Acoustic Metamaterials. Physical Review Applied. 8(1):014029-1-014029-12. doi:10.1103/PhysRevApplied.8.014029

Visco-thermal losses in double-negative acoustic metamaterials

Vicente Cutanda Henríquez*
Center for Acoustic-Mechanical Micro System, Technical University of Denmark, DK-2800, Kgs. Lyngby, Denmark

Victor M. García-Chocano, José Sánchez-Dehesa†
Wave Phenomena Group, Universitat Politècnica de València, Camino de Vera s.n. (Building 4D), ES-46022 Valencia, Spain
(Dated: June 11, 2017)

The influence of losses in double-negative metamaterial slabs recently introduced by Graciá-Salgado and coworkers [see Phy. Rev. B, 88, 224305 (2013)] is here comprehensively studied. Viscous and thermal losses are considered in the linearized Navier-Stokes equations with no flow. Despite of the extremely low thicknesses of boundary layers associated to each type of losses, the double-negative behavior is totally suppressed for the rigid structures under analysis. In other words, almost 100% of the transmitted energy into the slab is dissipated by visco-thermal effects, in agreement with experimental data. Simulations undertaken for larger structures, using scale factors up to 20 times, show that double-negative behavior is never recovered. The huge dissipation obtained by these structures leads us to propose them as interesting alternatives to conventional absorbers for specific situations, e.g. when treating low frequencies or when the excitation is narrow banded.

PACS numbers: 43.20.+g;41.20.Jb;42.25.FX
Keywords: acoustic metamaterials, negative refraction, negative bulk modulus, negative mass density

I. INTRODUCTION

The engineering of robust artificial structures, named acoustic metamaterials [1–4], capable of exhibiting a negative-index of refraction is still an open task. Negative refraction can be obtained as a consequence of band folding effects in periodic structures made of sound scatterers [5]. But here we are interested in negative-index structures based on metamaterials with both the bulk modulus and the mass density negative. Metamaterials exhibiting dynamical mass density with negative values were first demonstrated using structures of metallic spheres embedded in an epoxy matrix[6]. This extraordinary behavior was explained as a consequence of the dipole-type resonance excited in the structure by the propagating wave. After this finding, double negative metamaterials were proposed[7] based on the possibility of having scatterers with monopolar resonances, which were the responsible of showing a negative dynamical bulk modulus. Metamaterials with negative bulk modulus were soon demonstrated using a variety of artificial structures[8–11]. Artificial structures behaving as double-negative metamaterials have been proposed in the last decade[7, 12–18], but only a few have been experimentally demonstrated[14, 19, 20]

An important issue regarding the practical functionality of negative-index metamaterials based on rigid or solid structures is the presence of unavoidable viscous and thermal boundary layers at the solid-fluid interface, leading to non negligible losses. These losses, not considered on the design procedure, might produce the suppression of the negative-index behavior. Recently, a few papers have investigated boundary layers effects in metamaterials. For example, Frenzel *et al.*[21] demonstrate that losses in labyrinthine metamaterial structures are very significant, making them as an interesting option for subwavelength broadband and all angle acoustic absorbers. Guild *et al.*[22] have proposed anisotropic metamaterials broadband absorbers based on the effects of viscous and thermal boundary layers on sonic crystals with filling fractions much larger than traditional porous absorbers. More recently, Moleron *et al.*[23] demonstrated that visco-thermal losses avoid completely the excitation of Fabry-Perot resonances. Previously, Theocaris and coworkers[24] have shown that formation of near-zero group velocity dispersion bands are hindered by visco-thermal dissipation. However, in Ref. [22] visco-thermal losses have been exploited to design specific metamaterials with absorption enhancement and showing a strongly anisotropic dissipation .

In this work we study the influence of visco-thermal losses in acoustic metamaterials based on rigid structures with predicted double negative behavior[25, 26]. The experimental characterization of these structures has shown that the double-negative structure lost its expected perfect transmission feature. This work has the purpose of clarifying this experimental findings by including in the theoretical analysis the effects of visco-thermal boundary layers.

The article is organized as follows. After this introduction, in Sec. II, we give a brief account of the theoretical design of the structures under study and the models employed in their simulations: the boundary element method (BEM) and the finite element method (FEM). Both are here improved in order to tackle the effect of

*Electronic address: vcuhe@elektro.dtu.dk
†Electronic address: jsdehesa@upv.es

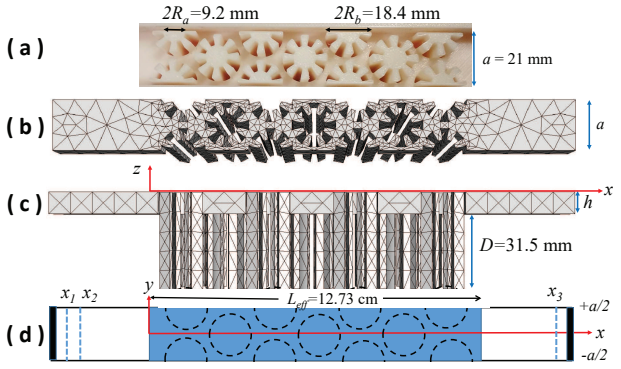

FIG. 1: (a) Top view of the metamaterial sample under study in this work. It was made in ABS plastic by a 3D printer. An array of anisotropic scatterers is embedded in a 2D waveguide with height h. (b) The corresponding BEM mesh version of the sample. An individual scatterer consists of a structured cylinder with radius R_b and total length $D + h$, where D is the depth of the wells drilled in the 2D waveguide. (c) Lateral view of the mesh employed in the BEM calculations. (d) Scheme of the waveguide showing the effective dimension, L_{eff}, of the metamaterial and the measurement positions (x_1, x_2, x_3).

visco-thermal losses in corrugated structures. Results of the numerical simulations are presented in Sect. III, giving a comprehensive discussion about the absorptive properties of Sample A characterized in Ref. [26]. Emphasis is put on the fact that absorptive properties of Fabry-Perot resonances depend on the symmetry of the band and on the group velocity. Section IV looks for the possibility of decreasing the visco-thermal losses by increasing the dimensions of the structure, showing that such approach is useless. Finally, the work is summarized in Sec. V.

II. THEORETICAL DESIGN AND NUMERICAL MODELING

The double-negative metamaterial under study is based in a theoretical design introduced in Ref. [25]. In brief, the unit cell consisted of a cylindrical cavity of depth D and radius R_b that is drilled into a waveguide with height h. In addition, a rigid cylinder of radius R_a is placed at the center of the cavity and is surrounded by eight rigid fins, which define a metafluid shell with dynamical mass $\rho_s < \rho_b$ and effective sound speed $c_s < c_b$, where ρ_b and c_b are, respectively, the static density and the phase velocity of the air background. In this work, the values assigned to these parameters in the calculations are ρ_b =1.199 kg/m^3 and c_b =343.99 m/s, corresponding to the air with static pressure of 101.325 KPa, temperature of 20^{o}C and humidity of a 50%. For the practical realization of the metamaterial, the fluid-like shell was manufactured using an equally partitioned structure made of eight rigid zones separated by eight air spacers, as shown in Figs. 1(a)-(c).

With the unit cell described above, the negative bulk modulus is attained thanks to the cavity drilled in the waveguide [11]. This cavity plays the same role than Helmholtz resonators, which have been previously shown to attain negative effective bulk modulus in a 1D water-filled waveguide [8]. On the other hand, the structured shell provides the dipolar resonance necessary to attain negative density values near resonance[6].

Figure 1(a) is a photo showing a top view of the metamaterial sample A characterized in Ref. [26]. This structure is here analyzed by two different numerical algorithms that consider the thermal and viscous losses of this man made structure. The remaining of this section gives a brief description of their main features.

A. BEM with losses

The Boundary Element Method here employed is based on the Kirchhoff derivation of the Navier-Stokes equations [27, 28].

$$(\Delta + k_a^2)p_a = 0 \quad (1)$$
$$(\Delta + k_h^2)p_h = 0 \quad (2)$$
$$(\Delta + k_v^2)\vec{v}_v = 0, with\ \Delta \cdot \vec{v}_v = 0, \quad (3)$$

where indexes (a, h, v) define the the acoustic, thermal and viscous modes, which are treated independently in the acoustic domain and linked through the boundary conditions. The time dependence $e^{i\omega t}$ is assumed, where ω is the angular frequency.

The acoustic, thermal and viscous wavenumbers k_a, k_h and k_v are expressed as:

$$k_a^2 = \frac{k^2}{1 + ik(\ell_v + [\gamma - 1)\ell_h] - k^2\ell_h(\gamma - 1)(\ell_h - \ell_v)} \quad (4)$$
$$k_h^2 = \frac{-ik}{1 - ik(\gamma - 1)(\ell_h - \ell_v)} \quad (5)$$
$$k_v^2 = -\frac{i\rho_0 ck}{\mu}, \quad (6)$$

where ρ_0 is the static density of air, c is the speed of sound, k is the adiabatic wavenumber and γ is the ratio of specific heat at constant pressure and specific heat at constant volume C_p/C_v. The viscous and thermal characteristic lengths are $\ell_v = (\eta + 4/3\mu)/\rho_0 c$ and $\ell_h = \lambda/(\rho_0 c C_p)$, where λ is the thermal conductivity, μ is the coefficient of viscosity and η is the bulk viscosity or second viscosity.

The velocity has contributions from the three modes $v = v_a + v_h + v_v$ while the total pressure is the sum of only the acoustic and thermal components, $p = p_a + p_h$ (the viscous mode has no pressure associated). Note that Eqs. (1)-(3) define a total of five equations with five unknowns; while Eq. 1 is a wave equation, Eqs. 2 and 3 are diffusion equations.

The BEM with losses is based on research software [29]. The calculation obtains the acoustic component of

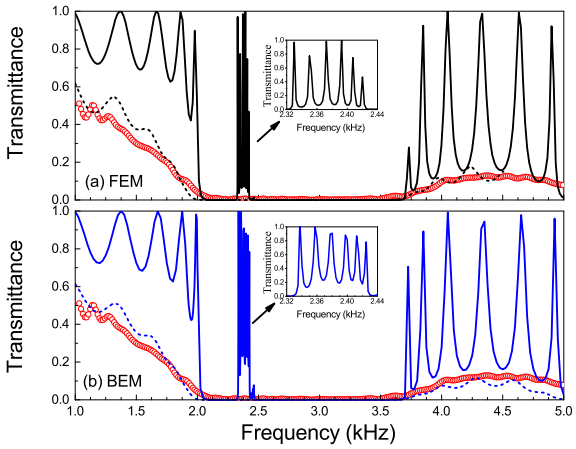

FIG. 2: (a) Transmittance spectra obtained from FEM simulations. Results obtained with no-losses (continuous lines) are compared with those including visco-thermal losses (dashed lines). (b) Transmittance spectra obtained from BEM simulations. Results obtained with no-losses (continuous lines) are compared with those considering visco-thermal losses (dashed lines). The symbols in both plots represents the experimental data.

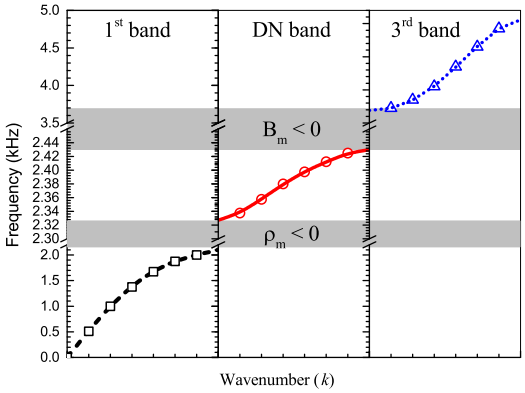

[t]

FIG. 3: Acoustic band structure obtained from the Fabry-Perot peaks (symbols). The dispersion relation is represented along the propagation direction; that is, along the direction ΓJ of the hexagonal lattice. It is displayed using the scheme of extended zone. Breaks are used in order to visualize the narrow double negative band. The shadow regions define the bandgaps with single negative behavior.

the pressure, p_a in Eq. (1), on the boundary. From this result, the remaining magnitudes are deduced using extended visco-thermal boundary conditions [30]. The final step is the calculation on domain points away from the boundary, such as those where the sound pressure is sampled in the waveguide, (x_1, x_2, x_3) in Fig. 1

The calculation here performed has been improved with respect to that reported in Ref. [31]. The Boundary Element mesh is obtained using the Gmsh grid generator [32]. The mesh describing the metamaterial, which is shown in Fig. 1(b) and 1(c), contains 9616 nodes in 4810 quadratic 6-node triangular surface elements. A total of 210 frequencies per setup were calculated in the range 1000 to 5000 Hz, with a spacing that varies from 2.5 Hz in relevant frequency zones, such as Fabry-Perot modes and bulk modulus resonances, to 100 Hz over slowly varying frequency regions.

B. FEM with losses

Corresponding FEM simulations are performed using the commercial software COMSOL. The full linearized Navier-Stokes description is employed. The equations solved are the momentum, continuity and energy equations [33].

The geometry of the structure to be solved is shown schematically in Fig. 1(d), where dark areas at both ends of the waveguide represent Perfectly Matched Layers (PML). Excitation of the waveguide is done though a body force with a small gap of air followed by a PML in order to guarantee full absorption at the inlet of waves reflected back from the metamaterial. A second PML is set at the receiving end to simulate an infinite waveguide.

The FEM calculation is computationally very demanding [31], and is only used in this work as a verification. Most of the calculations are performed using BEM.

III. RESULTS AND DISCUSSION

The parameter dimensions of the double-negative structure analyzed correspond to that of sample A in Ref. [26]; that is, R_b =9.2 mm; R_a =4.6 mm; L =31.5 mm; and a =21 mm. The three-point technique has been here employed to obtain the complex transmittance and reflectance of the metamaterial slab. Figure 1(d) shows a schematic view of the experimental setup inside the waveguide; x_i defines the positions of microphones and the dashed circles represent the metamaterial units defining the slab, with effective length L_{eff}. This length defines the separation between surfaces of the slab. Since the surface of the metamaterial is not well defined, we have employed the criteria applied in semiconductor physics and successfully applied to sonic crystal slabs (see, for example, Ref. [34]). Thus, we have considered that the metamaterial surface is located at one half of the separation between consecutive layers in the slab. The sample shown in Fig. 1(a) consists of seven layers with layer separation of $a\sqrt{3}/2$. Therefore, $L_{eff} = a3.5\sqrt{3}$, which is equal to 12.73 cm for the lattice constant a =21 mm. The origin of coordinates, x =0, along the propagation direction defines the position of the slab left surface in Fig. 1(d). With this origin, the positions of the three sample points (x_1, x_2, x_3) are respectively -4.18 cm, -3.84 cm and 16.91 cm. The rectangular waveguide is termi-

nated with ρc acoustic impedance at both ends in order to avoid reflections and simulate an infinite length. The excitation end is a piston termination with a velocity amplitude $(\rho c)^{-1}$, so that the undisturbed progressive plane wave can have a pressure amplitude of one.

The frequency dependent reflection and transmission factors are, respectively:

$$r(\omega) = \frac{P_2 e^{-ik_0 x_1} - P_1 e^{-ik_0 x_2}}{P_1 e^{ik_0 x_2} - P_2 e^{ik_0 x_2}} \quad (7)$$

$$t(\omega) = \frac{P_3}{P_2} \cdot \frac{e^{-ik_0 x_2} + r(\omega) e^{ik_0 x_2}}{e^{-ik_0 x_3}} e^{-ik_0 L_{eff}}, \quad (8)$$

where P_1, P_2 and P_3 are the pressure values obtained at the three sample points x_i.

In absence of any type of losses, energy conservation implies that the sum of power transmittance, $T(\omega) = |t(\omega)|^2$, and reflectance, $R(\omega) = |r(\omega)|^2$, should be unity for any frequency. This condition has been used as a measure of the accuracy of the calculation method. It was found that the best method for obtaining the pressure at the prescribed x_i positions is a mean of the pressures calculated over a $x-$constant plane inside the waveguide. Three 2×5 grids of regularly spaced field points were used to this purpose. With this method, the deviation from the expected sum of transmittance and reflectance was below 2×10^{-3} in most of the frequency range, only reaching 2×10^{-2} to 0.8×10^{-2} at the Fabry-Perot resonances. These values are considered rather satisfactory, given that transmittance and reflectance vary in a range between 0 and 1.

In the presence of viscous and thermal losses, the dissipated energy (absorptance) is calculated from,

$$A(\omega) = 1 - R(\omega) - T(\omega) \quad (9)$$

Figures 2(a) and 2(b) report the power transmittance, using the FEM and BEM algorithms. The continuous lines represent the spectra obtained without considering losses, while the dotted lines correspond to results obtained including losses. The peaks in the spectra represent Fabry-Perot (FP) resonances which appear due to the finite size of the sample. In addition, the calculated spectra corresponding to the case with losses included are in excellent agreement with the measured profiles, represented as symbols in Figs. 2(a) and 2(b). Both algorithms predict the suppression of the narrow band associated to double-negative behavior. Finally, Fig. 2 supports the equivalence between both numerical algorithms, both giving results with the same accuracy and reproducing the experimental data when visco-thermal losses are included.

1. *lossless case*

For the case of no losses included (continuous lines), both algorithms predict the existence of a narrow band between 2.33 kHz and 2.44kHz, corresponding to the

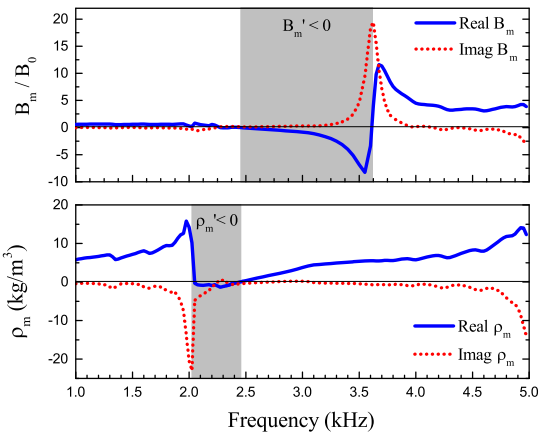

FIG. 4: (Color online) Frequency dependence of the effective parameters of the metamaterial, bulk modulus (B_m) and density (ρ_m), respectively. They are obtained using the procedure described in Ref. [35].

presence of double-negative behavior. Unity transmission is obtained at frequencies corresponding to FP peaks, where the thickness of the sample is commensurate with an integer number m of half wavelength; i.e., at $f \approx mc_b/(2L_{eff})$.

It is well known that frequencies of FP modes can be employed to reconstruct the acoustic bands along the propagation direction[34], the ΓJ direction of the hexagonal lattice in this case. Regarding the spectrum below 2.05 kHz, the band edge of the first pass band, Fig. 2 shows that FP modes produce peaks with decreasing bandwidth; i.e., a FP peak closer to the upper band edge exhibits narrower bandwidth than that with lower frequency. Moreover, the distance between peaks also decreases near the band edge. Since both effects are directly related to the band dispersion relation, it is expected that the acoustic band has a strong curvature near the edge. However, Fig. 2 shows that for the transmission band corresponding to double negative behavior (2.33kHz $< f <$ 2.44 kHz) the associated FP modes have almost the same bandwidth and equal separation between them, indicating that the associate band should be almost flat. For the third transmission band (above 3.7 kHz) we observe again that the modes near the edges are narrower than in the central region of the band.

Figure 3 shows the acoustic bands reconstructed from the FP peaks using the extended zone scheme. The symbols represent the FP peaks in the different pass-band regions and the lines represent the fitted dispersion relation of the bands.

2. *visco-thermal effects*

When visco-thermal effects are included, numerical simulations shown in Fig. 2 (short dashed lines) in-

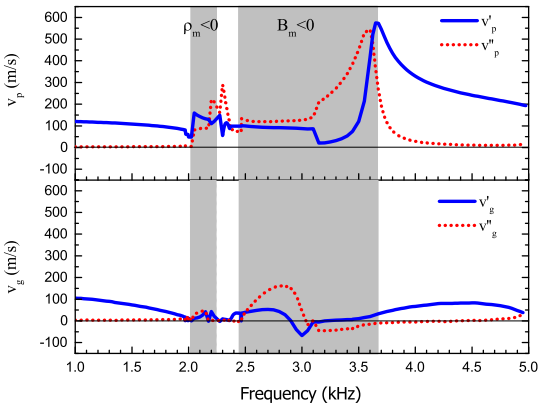

FIG. 5: (Color online) Components of the extracted phase velocity (v_p) and group velocity (v_g) for the metamaterial where the visco-thermal effects are considered. The shadowed zones define the regions where the metamaterial is single negative according to results shown in Fig. 2.

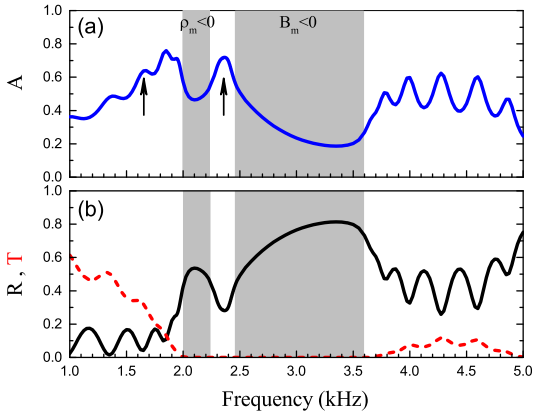

FIG. 6: (a) Frequency dependence of the power loss (Absorptance) for the double-negative metamaterial under study. (b) The corresponding behavior for the Reflectance and the Transmittance. The shadowed zones define the regions where the metamaterial is single negative according to results shown in Fig. 2.

dicate that, at any frequency, transmittance values are much lower than those obtained without losses (continuous lines). It is observed that FP peaks in the bands below 2 kHz and above 3.8 kHz strongly decrease and their frequencies are downshifted as a consequence of losses. Moreover, FP peaks in the miniband associated to double-negative behavior (see the insets) are completely suppressed due to visco-thermal effects. The excellent agreement observed between measurements (symbols) and simulations supports the conclusion that visco-thermal dissipation is the leading mechanism controlling the propagation features through the metamaterial sample. To further support this conclusion, we have calculated the effective bulk modulus and density components, which have been extracted from simulations on this metamaterial using the reflection/transmission (RT) method[35]. Figure 4 shows the extracted metamaterial parameters, B_m and ρ_m, which are complex due to the losses. Note that the real component of bulk modulus, B'_m, is negative for frequencies between 2.45 kHz and 3.6 kHz. On the other hand, the real component of the mass density, ρ'_m, is negative for frequencies between 2.05 and 2.45 kHz. Therefore, when visco-thermal effects are considered, the RT method is unable to give a frequency region where both effective parameters are simultaneously negative.

When density and bulk modulus are complex, the phase velocity v_p becomes complex.

$$v_p = \sqrt{\frac{B_m}{\rho_m}} = \sqrt{\frac{\rho'_m B'_m + B''_m \rho''_m - i(\rho''_m B'_m - \rho'_m B''_m)}{\rho'^2_m + \rho''^2_m}} = v'_p + iv''_p \quad (10)$$

Single prime in this equation denote real components and double primes denote imaginary components. In addition, the components of the group velocity can be obtained from v_p through the following relationship,

$$v_g = v_p[1 - \frac{\omega}{v_p}\frac{dv_p}{d\omega}] = v'_g + iv''_g \quad (11)$$

The components of both velocities are shown in Figs. 5(a) and 5(b), respectively. First, Fig. 5(a) shows that the real component of the phase velocity, v'_p, is positive in the frequency region between 2.2 and 2.45kHz, corresponding to the region where double-negative behavior is expected (see Figs. 2 and 3). This property for v'_p leads us to conclude that the real component of the effective refractive index is positive ($n' > 0$). In addition, the imaginary component, v''_p, in the same frequency region is not negligible, implying a damping of the propagating wave due to visco-thermal losses. In the regions with single-negative behavior, the existence of imaginary components causes phase distortion of evanescent waves. Regarding v_g, Fig. 5(b) indicates that the real component, v'_g takes extremely low values in the double negative region, which is consistent with the flat band observed in Fig. 3.

The decreasing of the transmittance profile can be explained from the results obtained for the calculated dissipated energy and reflectance, which are shown in Figs. 6(a) and 6(b), respectively. On the one hand, in the region with expected negative refractive index, it is observed that around a 30% of the impinging energy is reflected while a 70% is absorbed; in other words, the transmitted energy into the metamaterial slab is totality dissipated by visco-thermal effects. On the other hand, in the passbands regions (i.e., below 2 kHz and above 3.6 kHz) it is observed that maximum absorption is produced at the frequencies of the FP resonances.

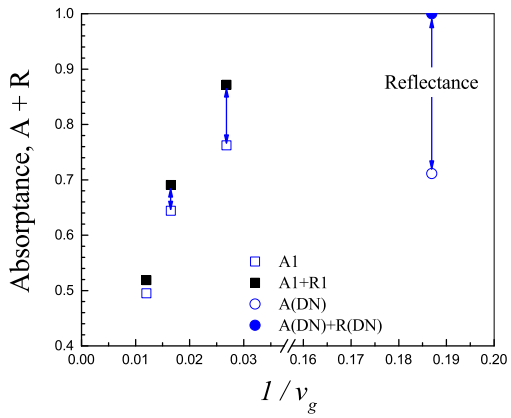

FIG. 7: (a) Absorptance of FP peaks (hollow symbols) as a function of the reciprocal of the group velocity, v_g. Values in the first passband (squares) and the double-negative band (circles) are shown. The full symbols represent the addition of Absorptance (A) and Reflectance (R) at the frequency of the FP resonance.

The effects of visco-thermal losses on Fabry-Perot resonances has been already discussed by Moleron and coworkers[23] on metamaterial structures made of periodic slits, where they demonstrate that the resonance peaks exhibit a strong attenuation as the effective length of the metamaterial increases. In this work, employing a metamaterial with fixed length L_{eff}, we have concluded that the strength of visco-thermal effects depends on the symmetry of the FP modes together with the value of the group velocity at the frequency of the FP resonance. This effect is shown in Fig. 7, which presents the absorptance (hollow symbols) at the FP frequencies. The peaks in the first passband (squares) and the double-negative band (circles) are shown as a function of the reciprocal of the group velocity v_g. The full symbols represent the addition of absorptance peaks and reflectance deeps observed in Fig. 6. For the FP resonances within the first pass-band (hollow squares), its is observed that the absorptance is almost linearly dependent on the reciprocal of v_g. In addition, the reflectance (double arrow) is larger for lower v_g. The latter effect is a consequence of the larger mismatch of impedance between the metamaterial and the air background when v_g decreases. For the FP resonances corresponding to the double-negative band, the absorptance is extraordinary, leading to the total suppression of the transmitted signal; i.e., $A + R \approx 1$, corresponding to almost a 100% absorption of the signal transmitted into the metamaterial slab. The key difference between both dissipative phenomena arises from the differences in the symmetry of the propagating modes. The modes propagating in the first pass band have plane wavefronts, the corresponding FP resonances are standing waves whose nodes are planes perpendicular to the propagating direction. On the contrary, the modes belonging to the double-negative narrow band are obtained

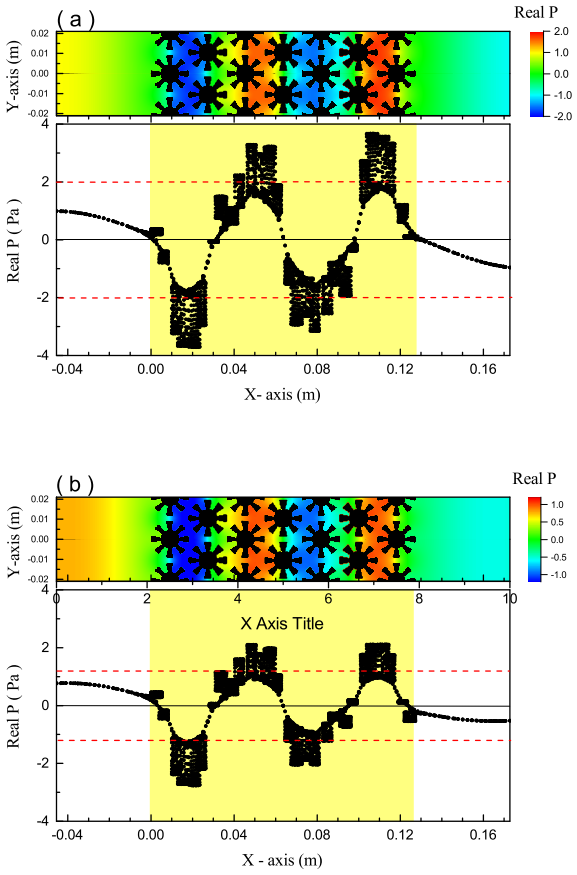

FIG. 8: Snapshots of the calculated pressure (real part) at 1675 kHz. Pressure values (in Pascals) are shown along the waveguide for a wave traveling from left to right, and for the two cases of interest: (a) without losses, and (b) with losses. The upper panels show the pressure patterns calculated at the top surface of the waveguide (z =0) while the lower panels plot the pressure values along the $x-$axis. The yellow region defines the boundaries of the metameterial slab. The horizontal dashed lines are guides for the eye. For animations of the instantaneous fields, see Video 1 and Video 2

from linear combinations of monopolar and dipolar resonances. So, large oscillations of the pressure amplitudes are achieved at the position of the metamaterial building units, where the dissipation is strongly enhanced due to the extraordinarily low v_g.

In order to get a better physical insight of the phenomena discussed above we have conducted a series of BEM simulations at several frequencies, corresponding to FP resonances: inside the first pass band and inside the double-negative band. In what follows we discuss two representative examples.

The behavior of a propagating wave with frequency of 1.675 kHz, within the first pass band, is shown in Figs. 8(a) and 8(b) for the cases without losses and with losses, respectively. This frequency corresponds to the FP peak indicated by the left arrow in Fig. 6. The calculated

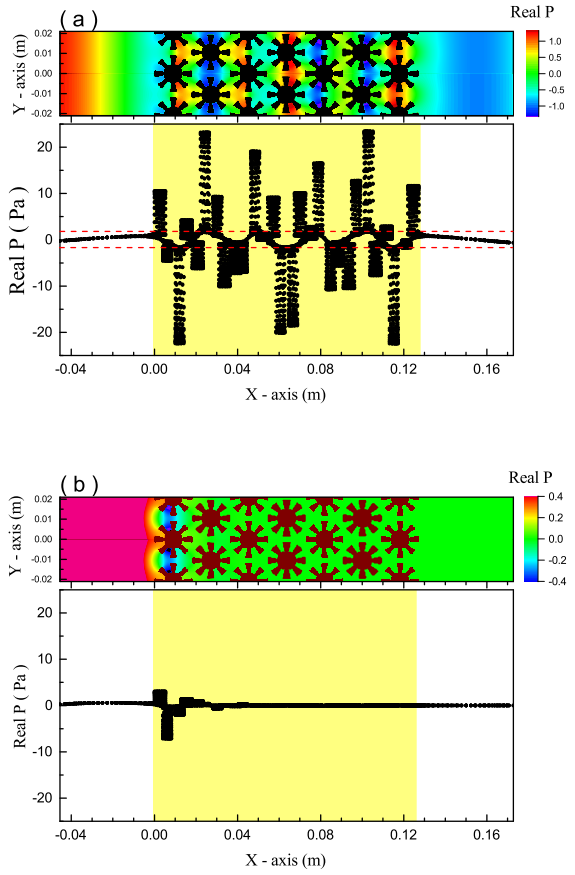

FIG. 9: Snapshots of the calculated pressure (real part) at 2380 kHz. Pressure values (in Pascals) are shown along the waveguide for a wave traveling from the left to the right, and for the two cases of interest here: (a) without losses, and (b) with losses. The frequency corresponds to the third Fabry-Perot peak obtained inside the double-negative band. The upper panels show the pressure patterns calculated at the top surface of the waveguide (z =0) while the lower panels plot the pressure values along the $x-$axis. The yellow region defines the boundaries of the metameterial slab. The horizontal dashed lines are guides for the eye. For animations of the instantaneous fields, see Video 3 and Video 4

values are displayed in two different manners. The upper panels represent the pressure patterns obtained at the top surface of the waveguide (i.e., at $z = 0$); it is a surface plot where the values are given in a color scale. The lower panels give the pressure obtained along the $x-$axis, the black dots represent values obtained at different (y, z) positions in the structure. Results corresponding to the lossless case are given in Figs. 8(a), where the surface plot indicates that the propagating wave has plane wavefronts in which the pressure amplitude oscillates between -2 and +2. The plot representing real P along $x-$axis can be understood as a combination of values corresponding to points inside the waveguide (i.e., for $-h < z < 0$ and $-a/2 \leq y \leq +a/2$), and values associated to points inside the air cavities of the metamaterial units (i.e. at positions where $-h \leq z \leq -h+D$). When visco-thermal losses are included, panels in Fig. 8(b) show that the previous behavior is basically maintained, the main difference being just a uniform decreasing of the pressure values along the metamaterial slab. So, the impinging signal finally arrives at the opposite end with an energy attenuated by an amount of around 65% (see Fig. 6). In both figures, the horizontal dashed lines define the maximum values taken by the pressure inside the waveguide. Motion pictures showing the time evolution of the calculated pressure amplitude along the waveguide at the frequency of 1.675 kHz are presented in Videos 1 and 2.

Results obtained for a wave with frequency 2.38 kHz, within the narrow band with double negative behavior, are shown in Figs. 9(a) and 9(b) for the case without and with losses, respectively. This frequency corresponds to the FP resonance indicated by the right arrow in Fig. 6. In comparison with results obtained for the FP inside the first passband, we observe two main differences. For the case without losses, the upper panel in Fig. 9(a) shows that the pressure pattern does not represent a wave with plane wavefronts. Instead, the pressure variations appear around the building units. In addition, the variation of the pressure significantly increases within the unit cavities, as it is shown in the plot (Real P) versus x. As in the lower panels of Fig. 8, the horizontal dashed lines define the maximum values taken by the pressure in the waveguide. When the viscous and thermal losses are included, Figs. 9(b) show that the traveling wave is strongly attenuated in just a few rows of the metamaterial slab; the pressure being negligible after the third row. This behavior can be explained in terms of the strong dissipation taking place locally, in the individual units along the metamaterial, a phenomenon which is enhanced due to the fact that the group velocity of modes in this band is extraordinarily low (see Fig. 5(b)). Motion pictures showing the time evolution of the calculated pressure amplitude along the waveguide at the frequency of 2.38 kHz are presented in Videos 3 and 4.

IV. SCALING OF THE METAMATERIAL

The viscous boundary layer has a characteristic length $\delta_v = \sqrt{\frac{2\nu}{\omega\rho_0}}$, where ν is the coefficient of shear viscosity and ρ_0 the air density. Simultaneously, the thermal boundary layer formed as a consequence of the heat transfer between the air and the rigid walls in the structure has a characteristic length $\delta_\kappa \approx \sqrt{\frac{2\kappa}{c_p\rho_0\omega}}$, where κ is the thermal conductivity and c_p is the specific heat at constant pressure [27]. For the measurement temperature and the operational frequency of 2.38 kHz, the thicknesses of viscous and thermal boundary layers are calculated to be 42 microns and 49 microns, respectively. These values are less than 2% of the minimum separation, d, between building units in the metamaterial lattice;

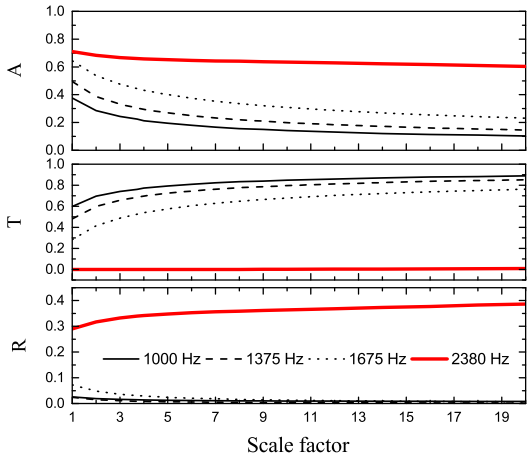

FIG. 10: Behavior of reflectance (R), transmittance (T) and absorptance (A) as a function of the scale factor for frequencies corresponding to Fabry-Perot peaks at the first band (black thin lines) and at the double-negative band (red thick lines).

$d = 2R_{ext} - a$. This value is lower than the $\approx 5\%$ threshold that was recently demonstrated to impact acoustic performance in small channels[36]. Regarding the separation between walls inside a building unit, the minimum distance is given by $2\pi R_a/16$. The values δ_v and δ_κ are only a 2.3% and a 2.7%, respectively, of this minimum separation (1.8 mm).

Taking into account that $\delta_v/d = 2.2 \times 10^{-3}/\sqrt{a}$, we have further reduced the percentage of the boundary layers in relation to the smallest separation between scatterers by just applying a scale factor to all dimensions of the metamaterial. Results for metamaterial slabs with effective lengths from L_{eff} =127.5 mm, until L_{eff} =2.55 m, corresponding to scale factors from 1 to 20, are here presented and discussed. For the lossless case, BEM simulations show that transmittance spectra are the same but frequency shifted by the corresponding scale factor. Instead, when visco-thermal losses are included, the spectra do not scale in the same way since the thicknesses of the viscous and thermal boundary layers are inversely proportional to $\sqrt{f}$. Moreover, viscous losses strongly depend on the incident angle.

Figure 10 shows the behavior of reflectance, transmittance and absorptance corresponding to FP peaks in the first passband (black thin lines) and one belonging to the DN band (blue thick lines). They are obtained at four frequencies (indicated in the figure) that are divided by the scale factor as the sample is scaled up. Two types of behavior are clearly observed. For the FP peaks emerging from the first passband, the absorptance strongly decreases with increasing scale factors; maximum absorption is obtained for the FP peak at 1675 Hz, the one with lower group velocity. For this structure the scale factor has a relevant contribution to decrease the visco-thermal losses or, equivalently, to enhance the transmitted power. However, for the FP peak inside the DN band, it is observed that an increase of the dimensions by a factor of 20 produces a decreasing of the absorptance of a merely 9%; it goes from 71% to 60%. Curves also show that practically a 100% of the acoustic energy entering into the metamaterial slab is absorbed almost independently of the scale. From these simulations we conclude that acoustic energy transmitted at frequencies within the DN band is totally absorbed by the metamaterial slab. This conclusion forbids the use of these metamaterials for designing any device in which the properties of double-negativity are required. Instead, they can be employed in developing structures for total absorption at the frequencies where DN behavior is expected without losses.

V. SUMMARY AND CONCLUSIONS

In summary, we have presented a comprehensive study of viscous-thermal effects in quasi-2D artificial structures like the ones introduced in Ref. [26], which were designed to exhibit double-negative behavior. The building units consist of structured cylinders made of a rigid material having air cavities penetrating deeply in the waveguide. The reported experimental characterization of these type of metamaterial was unable to demonstrate any feature confirming double-negative effects. We have performed extensive numerical simulations based on the Boundary Element Method, which has been improved and adapted to tackle viscous-thermal losses in these metamaterial structures. We conclude that these structures are very efficient in absorbing the energy of acoustic waves traveling trough them. After studying a metamaterial slab of seven layers we arrive to several conclusions. On the one hand, for frequencies within the first passband, the absorbed energy reaches values as high as 80%, the amount of absorptance being directly proportional to the reciprocal of the group velocity in the band. However, for waves with frequencies within the double-negative region, the impinging wave is totally absorbed in the first few layers of the metamaterial slab as a consequence of the visco-thermal losses, which are enhanced due to the extremely low value of the group velocity inside this narrow band region. Finally, we have explored the possibility of reducing the relevance of losses by applying a scaling factor to the dimensions of the initial samples. Unfortunately, our results show that this approach is not able to restore the extraordinary features associated to double-negativity. So, the present study leads us to conclude that fin-based metamaterials structures are not able to exhibit the predicted double-negative behavior because of the strong dissipation associated to visco-thermal losses. A large amount of losses has also been reported in other rigid-based structures with embedded resonances [15, 20], where the lack of a significant signal in the transmitted energy made them unfeasible to develop practical devices. These results

may indicate that visco-thermal losses are relevant to any rigid-based double-negative metamaterials. Though further theoretical analysis should be performed in order to support this general conclusion, we speculate that rigid-based metamaterials structures could become interesting alternatives to conventional absorbers in particular situations, e.g. when treating low frequencies or when the excitation is narrow-banded, such as mufflers and low-frequency resonances in room acoustics.

Acknowledgments

V.M. G.-C. and J. S.-D. acknowledge the support from the Spanish Ministerio de Economía y Competitividad (MINECO), and the European Union Fondo Europeo de Desarrollo Regional (FEDER) through project No. TEC 2014-53088-C3-1-R.

Appendix

The temporal variation of the pressure field for a metamaterial slab showing double-negative behavior is demonstrated by Videos 1 to 4, which show sequences of snapshots taken along one period.

VIDEO 1. Motion pictures showing the behavior of total instantaneous pressure (real part) along the waveguide for the case of a wave with frequency 1.675 kHz, within the first passband. No losses are included in the calculation.

VIDEO 2. Motion pictures showing the behavior of the total instantaneous pressure (real part) along the waveguide for the case of a wave with frequency 1.675 kHz, within the first passband. Viscous-thermal losses are included in the calculation.

VIDEO 3. Motion pictures showing the behavior of the total instantaneous pressure (real part) along the waveguide for the case of a wave with frequency 2.38 kHz, within the double-negative passband. No losses are included in the calculation.

VIDEO 4. Motion pictures showing the behavior of the total instantaneous pressure (real part) along the waveguide for the case of a wave with frequency 2.38 kHz, within the double negative passband. Viscous-thermal losses are included in the calculation. Note that the impinging wave is completely absorbed by losses in just a few layers.

[1] S. Cummer, J. Christensen, and A. Alú, Controlling sound with acoustic metamaterials, Nat. Rev. **97**, 16001 (2016).
[2] G. Ma and P. Sheng, Acoustic metamaterials: From local resonances to broad horizons, Sci. Adv. **2**, e1501595 (2016).
[3] M. Haberman and M. D. Guild, Acoustic metamaterials, Physic Today **69**, 43 (2016).
[4] R. Craster and S. Guenneau, *Acoustic Metamaterials* (Springer, 2013), ISBN 0691024014.
[5] C. Hladky-Henon, J. Vasseur, G. Haw, C. Croenne, L. Haumesser, and A. Norris, Negative refraction of acoustic waves using a foam-like metallic structure, Appl. Phys. Lett. **102**, 144103 (2007).
[6] Z. Liu, X. Zhang, Y. Mao, Y. Zhu, Z. Yang, C. Chan, and P. Sheng, Locally resonant sonic materials, Science **289**, 1734 (2000).
[7] J. Li and C. T. Chan, Double-negative acoustic metamaterials, Phys. Rev. E **70**, 055602 (2004).
[8] N. Fang, D. Xi, J. Xu, M. Ambati, W. Srituravanich, C. Sun, and X. Zhang, Ultrasonic metamaterials with negative modulus, Nature mat. **5**, 452 (2006).
[9] S. H. Lee, C. M. Park, Y. M. Seo, Z. G. Wang, and C. K. Kim, Double-negative acoustic metamaterials, J. Phys.: Condens. Matter **21**, 175704 (2009).
[10] J. Fey and W. M. Robertson, Compact acoustic bandgap material based on subwavelength collection of detuned Helmholtz resonators, J. Appl. Phys **109**, 114903 (2006).
[11] V. García-Chocano, R. Graciá-Salgado, D. Torrent, F. Cervera, and J. Sánchez-Dehesa, Quasi two-dimensional acoustic metamaterial with negative bulk modulus, Phys. Rev. B **85**, 184102 (2012).
[12] Y. Ding, Z. Liu, C. Qiu, and J. Shi, Metamaterial with simultaneously negative bulk modulus and mass density, Phys. Rev. Lett. **99**, 093904 (2007), ISSN 1079-7114.
[13] Y. Cheng, J. Y. Xu, and X. Liu, One-dimensional structured ultrasonic metamaterials with simultaneously negative dynamic density and modulus, Phys. Rev. B **77**, 045134 (2008).
[14] S. H. Lee, C. M. Park, Y. M. Seo, Z. G. Wang, and C. K. Kim, Composite acoustic medium with simultaneously negative density and modulus., Phys. Rev. Lett, **104**, 054301 (2010).
[15] L. Fok and X. Zhang, Negative acoustic index metamaterial, Phys. Rev. B **83**, 214304 (2011).
[16] Z. Liang and J. Li, Extreme acoustic metamaterial by coiling up Space, Phys. Rev. Lett. **108**, 114301 (2012).
[17] Y. Xie, B. I. Popa, L. Zigonneau, and S. A. Cummer, Measurement of a broadband negative index with space-coiling metamterials, Phys. Rev. Lett. **110**, 175501 (2013).
[18] R. Graciá-Salgado, D. Torrent, and J. Sánchez-Dehesa, Double-negative acoustic metamaterial based on quasi-two-dimensional fluid-like shells, New J. Phys. **14**, 103052 (2012).
[19] T. Brunet, A. Merlin, B. Mascaro, and k. Zimny, Soft 3D acoustic metamaterial with negative index, Nat. Mat. **14**, 384 (2015).
[20] N. Kaina, F. Lemoult, M. Fink, and G. Lerosey, Negative refractive index and acoustic superlens from multiple scattering in single negative metamaterials, Nature **525**, 77 (2015).
[21] T. Frenzel, J. Brehm, T. Buckmann, R. Schittny, M. Kadic, and M. Wegener, Three-dimensional labyrinthine acoustic metamaterials, Appl. Phys. Lett. **103**, 061907 (2013).

[22] M. D. Guild, V. M. García-Chocano, W. Kan, and J. Sánchez-Dehesa, Acoustic metamaterial absorbers based on multilayered sonic crystals, J. Appl. Phys. **117**, 114902 (2015).

[23] M. Molerón, M. Serra-García, and C. Daraio, Visco-thermal effects in acoustic metamaterials:from total transmission to total reflection and high absorption, New J. Phys. **18**, 033003 (2016).

[24] G. Theocharis, O. Richoux, V. Romero-García, and V. Tournat, Limits of slow sound propagation and transparency in lossy, locally resonant periodic structures, New. J. Phys. **16**, 093017 (2014).

[25] R. Graciá-Salgado, D. Torrent, , and J. Sánchez-Dehesa, Double-negative acoustic metamaterial based on quasi-two-dimensional fluid-like shells, New J. Phys. **14**, 103052 (2012).

[26] R. Graciá-Salgado, V. García-Chocano, D. Torrent, and J. Sánchez-Dehesa, Negative mass density and density-near-zero quasi-two-dimensional metamaterial: Design and applications, Phys. Rev. B **88**, 224305 (2013).

[27] A. Pierce, *Acoustics. An introduction to its physical principles and applications (Ch.10)* (McGraw Hill, New York, 2013).

[28] M. Bruneau, P. Herzog, J. Keorgomarg, and J. Polack, General formulation of the dispersion equaition in bounded visco-thermal fluid, and applications to some geomteries, Wave Motion **11**, 441 (1989).

[29] V. Cutanda-Henríquez and P. Juhl, OpenBEM-An open source Boundary Element Method software in acoustics, Proc. Internoise 2010 (2010).

[30] V. Cutanda-Henríquez and P. Juhl, An axisymmetric boundary element formulation of sound wave propagation in fluids including viscous and thermal losses, J. Acoust. Soc. Am. **134**, 3409 (2013).

[31] V. Cutanda-Henríquez, P. R. Andersen, J. S. Jensen, P. M. Juhl, and J. Sánchez-Dehesa, A numerical model of an acoustic metamaterial using the boundary element method including viscous and thermal losses, J. Comp. Acoust. **25**, 1750006 (2016).

[32] C. Geuzaine and J.-F. Remacle, Gmsh: a three-dimensional finite element mesh generator with built-in pre- and post-processing facilities, Int. J. Num. Methods Engineering **79**, 1309 (2009).

[33] M. Malinen, M. Lyly, P. Råback, A. Kärkkäinen, and L. Kärkkäinen, A finite element method for the modeling of thermo-viscous effects in acoustics, Proc. 4th European Cong. Computational Methods in Applied Sciences and Engineering (2004).

[34] L. Sanchis, A. Håkansson, F. Cervera, and J. Sánchez-Dehesa, Acoustic interferometers based on two-dimensional arrays of rigid cylinders in air, Phys. Rev. B **67**, 035422 (2003).

[35] V. Fokin, C. Ambati, C. Sun, and X. Zhang, Method for retrieving effective properties of locally resonant acoustic metamaterials, Phys. Rev. B **76**, 144302 (2007).

[36] G. P. Ward, R. K. Lovelock, A. R. Murray, A. P. Hibbins, J. R. Samples, and J. D. Smith, Boundary-layer effects on acoustic transmission through narrow slit cavities, Phys. Rev. Lett. **115**, 044302 (2015).